PHYSICAL REVIEW A **97**, 052702 (2018)

Partial-wave analysis for positronium-xenon collisions in the ultralow-energy region

Kengo Shibuya[*] and Haruo Saito
Institute of Physics, Graduate School of Arts and Sciences, The University of Tokyo, Komaba 3-8-1, Meguro-ku, Tokyo 153-8902, Japan

(Received 7 February 2018; published 3 May 2018)

We propose a method to convert measured positronium annihilation rates in gaseous xenon into total and differential cross sections of positronium-xenon collisions in an ultralow-energy region of less than 80 meV where their experimental determinations as functions of the positronium kinetic energy are extremely difficult. This method makes it possible to determine not only the s-wave collisional parameters but also the p-wave and d-wave parameters. We have found a small positive value of the scattering length, $A_0 = 2.06 \pm 0.10\, a_0$, which indicates that the positronium-xenon interaction in this energy region is repulsive and suggests that it is dominated by the scattering amplitude of the positron rather than that of the electron. An extrapolation of the analytical result into the experimentally inaccessible energy regions from 80 meV to 1.0 eV indicates that there should not be a Ramsauer-Townsend minimum but rather a peak in the total cross section at an energy of approximately 0.4 eV.

DOI: 10.1103/PhysRevA.97.052702

I. INTRODUCTION

A positronium (Ps) atom is a hydrogenlike bound state of an electron and its antimatter, a positron. A Ps atom in a spin-triplet state is called "orthopositronium" (o-Ps, $S = 1$) and decays into three gamma-ray photons with a continuous spectrum (0–511 keV) with a lifetime of 142 ns in vacuum. A Ps atom in a spin-singlet state is called parapositronium (p-Ps, $S = 0$) and decays into two gamma-ray photons with a line spectrum (511 keV) with a lifetime of 125 ps in vacuum.

Ps atomic interactions with gas molecules have been intensively investigated by theoretical and experimental researchers for a long time [1–3]. Due to the small mass of a Ps atom, its de Broglie wavelength is often larger than collisional targets; e.g., it is 43 Å in thermodynamic equilibrium at room temperature. Much attention has been paid to whether low-energy Ps collisions exhibit characteristic quantum mechanical phenomena such as the Ramsauer-Townsend minimum, which is often observed in electron and positron scatterings [4].

Ps is a neutral particle, and its kinetic energy cannot be controlled by electric or magnetic fields. The energy region of 0.1–1 eV remains inaccessible to experimental methods. Above this energy region, experimentalists using monoenergetic Ps beams have found that the Ps scattering cross section is similar to the electronic scattering cross section [5–7], and theorists have argued that this similarity is due to the electron-exchange interaction playing a dominant role in Ps scatterings in the low- and intermediate-energy regions (1–100 eV) [8]. Below the inaccessible energy region, Ps in thermodynamic equilibrium with target gas molecules has been studied by measuring positron lifetime spectra (PLS) [9–11], Doppler broadening spectra [12–14], the angular correlations of the annihilation radiation, etc. [15–18]. Momentum-transfer cross sections for several targets have been reported. In this energy region, a similarity between Ps scattering and electron scattering is not expected because of the differences in the long-range interactions that control scattering; i.e., the van der Waals interaction for Ps scattering is considerably weaker than the polarization interaction for electron scattering.

The aim of the present study is to propose an analytical method to convert the experimental data of Ps annihilation rates into total and differential cross sections as functions of energy. Our method is based on a partial-wave expansion, which is suitable to describe the Ps spin-conversion annihilation that is forbidden in s-wave scattering ($L = 0$, where L is the orbital angular momentum of Ps toward the target nucleus). This selection rule enables experimental determinations not only of the s-wave scattering parameters but also of the p- and d-wave scattering parameters. These collisional parameters and their energy dependences are essential to describe whole positron transport codes because positrons often annihilate after creating Ps atoms [19,20]. We have validated the obtained parameters by simulating the PLS and have used them to extrapolate the total cross section from 80 meV to 1.0 eV where experimental access has not been achieved yet. The extrapolation indicates that there should not be a Ramsauer-Townsend minimum but rather a peak in the total cross section at an energy of approximately 0.4 eV.

II. THEORY AND METHODS

When a Ps atom is scattered by a high-Z atom such as xenon, the Ps spin state can be changed by the spin-orbit interaction, and spin conversions from o-Ps to p-Ps increase the annihilation rate and shorten the long lifetime [21–23]. As described below, this reaction is forbidden in s-wave scattering, and is dominated by p- and d-wave scatterings even in the ultralow-energy region. A partial-wave expansion analysis of this system makes it possible to determine not only the s-wave collisional parameters but also the p- and d-wave parameters owing to the selection rules. This is a unique advantage of the proposed method in comparison to electron scattering experiments in the ultralow-energy region [24,25].

---

[*] shibuken@gakushikai.jp

A. Ps spin conversion due to spin-orbit interactions

The Ps wave function (Φ) is described as the direct product of the spatial wave function ($\phi_{LM_l} = |L,M_l\rangle$) and the spin wave function ($\chi_{SM_s} = |S,M_s\rangle$), i.e., $\Phi = |L,M_l,S,M_s\rangle = |L,M_l\rangle|S,M_s\rangle$, where M_l is the z projection of L and M_s is the z projection of S. In detail, $|S,M_s\rangle$ can be described using the spin-up wave function (α) and the spin-down wave function (β) as $|1,1\rangle = \alpha_e\alpha_p$, $|1,-1\rangle = \beta_e\beta_p$, $|1,0\rangle = (\alpha_e\beta_p + \beta_e\alpha_p)/\sqrt{2}$, and $|0,0\rangle = (\alpha_e\beta_p - \beta_e\alpha_p)/\sqrt{2}$; hereafter the indices e and p denote the electron and positron, respectively. The state $|0,0\rangle$ corresponds to p-Ps and the other three states correspond to o-Ps.

Let the spin-orbit Hamiltonian ($\hat{H}_{\text{so}} = \xi\hat{l}\cdot\hat{s}$) act on Φ to figure out the matrix elements, where $\hat{l}$ and $\hat{s}$ are the angular momentum operator and the spin operator, respectively, and ξ is the spin-orbit coupling constant. For example, we obtain

$$\begin{aligned}
\hat{H}_{\text{so}}|L,M_l,1,1\rangle &= (\xi_e\hat{l}_e\hat{s}_e + \xi_p\hat{l}_p\hat{s}_p)\big|\phi_{LM_l}\big\rangle|\alpha_e\alpha_p\rangle,\\
\xi_e\hat{l}_e\hat{s}_e\big|\phi_{LM_l}\big\rangle|\alpha_e\alpha_p\rangle &= \xi_e\big(\hat{l}^x\hat{s}_e^x + \hat{l}^y\hat{s}_e^y + \hat{l}^z\hat{s}_e^z\big)\big|\phi_{LM_l}\big\rangle|\alpha_e\alpha_p\rangle\\
&= \xi_e\big[(\hat{l}^+\hat{s}_e^- + \hat{l}^-\hat{s}_e^+)/2 + \hat{l}^z\hat{s}_e^z\big]\big|\phi_{LM_l}\big\rangle|\alpha_e\alpha_p\rangle\\
&= \xi_e\hbar^2\{|\phi_{L(M_l+1)}\rangle[(|\alpha_e\beta_p\rangle + |\beta_e\alpha_p\rangle) - (|\alpha_e\beta_p\rangle - |\beta_e\alpha_p\rangle)]/\sqrt{2} + M_l|\phi_{LM_l}\rangle|\alpha_e\alpha_p\rangle\}/2\\
&= \xi_e\hbar^2(M_l|L,M_l,1,1\rangle + |L,M_l+1,1,0\rangle - |L,M_l+1,0,0\rangle)/2, \text{ and}\\
\xi_p\hat{l}_p\hat{s}_p\big|\phi_{LM_l}\big\rangle|\alpha_e\alpha_p\rangle &= \xi_p\hbar^2(M_l|L,M_l,1,1\rangle + |L,M_l+1,1,0\rangle + |L,M_l+1,0,0\rangle)/2.
\end{aligned} \tag{1}$$

The spin-orbit coupling operators in the x and y directions ($\hat{l}^x\cdot\hat{s}^x$ and $\hat{l}^y\cdot\hat{s}^y$, respectively) are replaced by the ladder operators ($\hat{l}^\pm = \hat{l}^x \pm i\hat{l}^y$ and $\hat{s}^\pm = \hat{s}^x \pm i\hat{s}^y$, respectively). In addition, $\phi_{LM'} = 0$ when $|M'| > L$. Equation (1) indicates that o-Ps ($|1,1\rangle$) can be converted into p-Ps ($|0,0\rangle$) because of the spin-orbit interaction.

Similarly, we obtain

$$\begin{aligned}
\hat{H}_{\text{so}}|L,M_l,1,-1\rangle &= \xi_e\hbar^2(|L,M_l-1,1,0\rangle - M_l|L,M_l,1,-1\rangle + |L,M_l-1,0,0\rangle)/2\\
&\quad + \xi_p\hbar^2(|L,M_l-1,1,0\rangle - M_l|L,M_l,1,-1\rangle - |L,M_l-1,0,0\rangle)/2,\\
\hat{H}_{\text{so}}|L,M_l,1,0\rangle &= \xi_e\hbar^2(|L,M_l-1,1,1\rangle + |L,M_l+1,1,-1\rangle + M_l|L,M_l,0,0\rangle)/2\\
&\quad + \xi_p\hbar^2(|L,M_l-1,1,1\rangle + |L,M_l+1,1,-1\rangle - M_l|L,M_l,0,0\rangle)/2, \text{ and}\\
\hat{H}_{\text{so}}|L,M_l,0,0\rangle &= \xi_e\hbar^2(-|L,M_l-1,1,1\rangle + M_l|L,M,1,0\rangle + |L,M_l+1,1,-1\rangle)/2\\
&\quad + \xi_p\hbar^2(-|L,M_l-1,1,1\rangle + M_l|L,M,1,0\rangle - |L,M_l+1,1,-1\rangle)/2.
\end{aligned} \tag{2}$$

The four-by-four matrix of the spin part of $\hat{H}_{\text{so}}$ ($\hat{V}_{\text{so}}$) can be described as

$$\hat{V}_{\text{so}} = \frac{\xi_e\hbar^2}{2}\begin{pmatrix} M_l & 0 & 1 & -1\\ 0 & -M_l & 1 & 1\\ 1 & 1 & 0 & M_l\\ -1 & 1 & M_l & 0 \end{pmatrix} + \frac{\xi_p\hbar^2}{2}\begin{pmatrix} M_l & 0 & 1 & 1\\ 0 & -M_l & 1 & -1\\ 1 & 1 & 0 & -M_l\\ 1 & -1 & -M_l & 0 \end{pmatrix}, \tag{3}$$

where the off-diagonal elements correspond to the spin conversion due to the spin-orbit interactions. If $M_l = 0$, conversions between $|1,0\rangle$ and $|0,0\rangle$ states are forbidden. In other words, ortho-para spin conversion occurs only when $M_l \geqslant 1$ and $L \geqslant 1$. The Hamiltonian $\hat{V}_{\text{so}}$ for p-wave scattering ($L = 1$) is illustrated in Fig. 1. The illustration indicates that a change in M_l by ± 1 is accompanied by a change in M_s by ∓ 1; the quantity $M_l + M_s$ is conserved during the spin conversion, and L does not change.

B. Ps spin conversion and pick-off annihilation rates

In the partial-wave analysis, a Ps atom incident as a plane wave is scattered by a central potential $V = U(r)$. An attractive potential pulls in the Ps wave and advances the phase, whereas a repulsive potential pushes out the Ps wave and delays the phase. The phase shifts (δ_L) contain information about the scattering. They can be considered for each L because the incident plane wave can be expanded as

$$\begin{aligned}
\psi_{\text{in}} &= \exp(i\mathbf{k}\cdot\mathbf{r}) = \exp(ikr\cos\theta)\\
&= \sum_{L=0}^{\infty}(2L+1)i^L j_L(kr)P_L(\cos\theta),
\end{aligned} \tag{4}$$

where j_L and P_L are spherical Bessel functions and Legendre polynomials, respectively. Then, δ_L can be described in the lowest-order approximation, called "shape-independent approximation," as

$$\cot\delta_L(k) = k^{-(2L+1)}\big(-A_L^{-1} + r_L k^2/2\big), \tag{5}$$

where k is the wave number, A_L are constants corresponding to the scattering amplitude (A_0 is called the "scattering length"), and r_L are constants corresponding to the range of potential (r_0 is called the "effective range") [26]. For the present analysis, we employ the higher-order approximation of δ_L for the potential $U(r) = \gamma^4 r^{-6}$, where γ is a constant with the dimension of

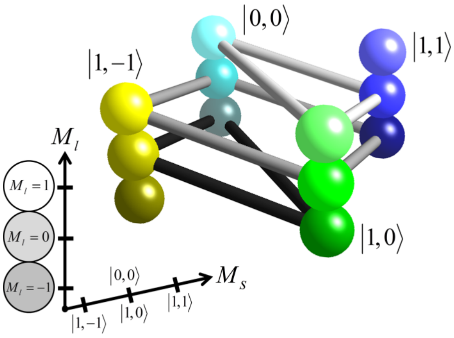

FIG. 1. Ps spin conversion due to the spin-orbit interaction during p-wave scattering ($L = 1$). Each sphere represents a Ps state; the magnetic quantum numbers are depicted on the vertical axis for the top spheres ($M_l = 1$), for the middle spheres ($M_l = 0$), and for the bottom spheres ($M_l = -1$), and the horizontal axis indicates M_s. A bar between any two spheres corresponds to a possible spin conversion. The bars and spheres form two triangles and one square; these three oblique planes represent the conservation law $M_l + M_s = \text{const.}$, as this quantity must be conserved throughout the spin-conversion reaction.

length, because Ps and xenon are both neutral particles and the dominant long-range interaction is a van der Waals force [27–29]. The derivations by Hinckelmann and Spruch ($L = 0$) [30], and by Ganas ($L = 1,2$) [31] give

$$\begin{aligned}\tan\delta_0(k) &\approx -A_0k - r_0A_0^2k^3/2 + \pi\gamma^4k^4/15\\ &\quad + 4A_0\gamma^4k^5\ln|2kd|/15,\\ \tan\delta_1(k) &\approx -A_1k^3 - r_1A_1^2k^5/2 + \pi\gamma^4k^4/35\\ &\quad + 4A_1\gamma^4k^7\ln|2kd|/35,\ \text{and}\\ \tan\delta_2(k) &\approx -A_2k^5 - r_2A_2^2k^7/2 + \pi\gamma^4k^4/315\\ &\quad + 4A_2\gamma^4k^9\ln|2kd|/315,\end{aligned} \tag{6}$$

where d is a specified distance over which the short-range potential identically vanishes. Using $\delta_L(k)$, one can describe the Ps-Xe total cross section (σ_{T}) and the momentum-transfer cross section (σ_{m}) as

$$\sigma_{\mathrm{T}}(k) = \frac{4\pi}{k^2}\sum_{L=0}^{\infty}(2L+1)\sin^2\delta_L(k) = \sum_{L=0}^{\infty}\sigma_L(k), \tag{7a}$$

and

$$\sigma_{\mathrm{m}}(k) = \frac{4\pi}{k^2}\sum_{L=0}^{\infty}(L+1)\sin^2[\delta_L(k) - \delta_{L+1}(k)], \tag{7b}$$

where $\sigma_L(k) = 4\pi k^{-2}(2L+1)\sin^2\delta_L(k)$ is the scattering cross section of the Lth partial wave [4,24,25]. The total cross section is the sum of the elastic scattering cross sections of the partial waves at energies less than the first excitation energy of Ps at 5.1 eV. There are no inelastic scatterings for noble-gas atoms in the ultralow-energy region because they have no vibrational or rotational degrees of freedom.

The normalized Ps annihilation rates via the two paths can be described using $\sigma_L(k)$ as

$$\begin{aligned}{}_1Z_{\mathrm{eff}}^{\mathrm{sc}}(k) &= \frac{c^3}{4\pi}f_{\mathrm{sc}}\int\rho(k)\left\{\sum_{L=1}^{\infty}\sigma_L(k)\right\}kdk,\ \text{and}\\ {}_1Z_{\mathrm{eff}}^{\mathrm{po}}(k) &= \frac{c^3}{4\pi}f_{\mathrm{po}}\int\rho(k)\left\{\sum_{L=0}^{\infty}\sigma_L(k)\right\}kdk,\end{aligned} \tag{8}$$

respectively, where c is the speed of light in vacuum, f_{sc} is the spin-conversion induced annihilation [hereafter, spin-conversion annihilation (SCA)] rate per collision, f_{po} is the pick-off annihilation (POA) rate per collision, and $\rho(k)$ is the wave-number distribution of o-Ps atoms. If Ps atoms are thermalized, a Maxwell-Boltzmann distribution [$\rho_{\mathrm{th}}(k)$] can be used as $\rho(k)$:

$$\rho_{\mathrm{th}}(k) = \frac{k^2}{\sqrt{\pi}}\left(\frac{1}{k_{\mathrm{B}}T}\right)^{3/2}\exp\left(-\frac{k^2}{4k_{\mathrm{B}}T}\right), \tag{9}$$

where k_{B} is the Boltzmann constant. Equations (5)–(10) are written in Hartree atomic units.

The measured energy dependence of the SCA and POA rates are analyzed using Eqs. (8) to obtain the collisional parameters. We can then calculate the differential cross section as

$$\frac{d\sigma}{d\Omega} = \left|\sum_{L=0}^{\infty}(2L+1)\frac{P_L(\cos\theta)}{k\cot\delta_L(k) - ik}\right|^2. \tag{10}$$

III. EXPERIMENT

The details of our measurement system have been described in our previous papers [22,32]. Briefly, a positron emitter, ^{22}Na (1.0 μCi), is sandwiched between silica aerogel (SAG) blocks (0.1 g cm^{-3}) that serve as positron-positronium converters in whose intergrain spaces the Ps atoms interact with xenon atoms [33–35]. This sandwich is placed at the center of a vacuum chamber that is wrapped with flexible heaters controlling the gas temperature, and the chamber is placed between the pole pieces of a conventional electromagnet controlling the static magnetic field. Two BaF$_2$ scintillation detectors for high-magnetic-field environments are placed near the chamber to detect both the 1.27-MeV gamma rays emitted from $^{22\mathrm{m}}$Ne immediately after the β^+ decay of ^{22}Na and the 0.511-MeV gamma rays emitted during pair annihilation. The detection signals are recorded using a digital oscilloscope, and the digitized waveforms are numerically analyzed to measure the time lag between the two signals and create the PLS [36,37]. The long-lifetime slope of the PLS is fitted with a single-exponential function after background subtraction to determine the lifetime. The typical fitting range is 170–400 ns after the prompt peak where the o-Ps atoms are considered to be thermalized [11].

We maintained the temperature at one of eight measurement points (T = 300, 363, 423, 483, 510, 540, 588, and 623 K), and we switched the magnetic field alternately on and off (B = 0.82 and 0.00 T, respectively) at hourly intervals. The gas pressure was 250 and 0 kPa; the PLS without xenon gas was also measured at each temperature point to determine the ${}_1Z_{\mathrm{eff}}^{\mathrm{po}}$

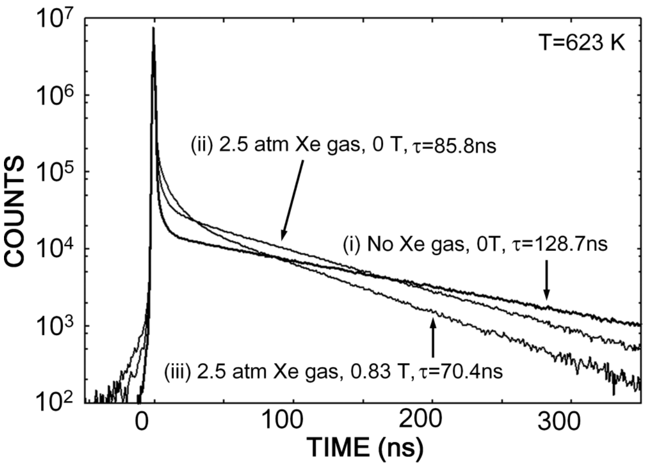

FIG. 2. Three positron lifetime spectra at 623 K: (i) with SAG and no xenon gas, (ii) with SAG and 250-kPa xenon gas, and (iii) with SAG and 250-kPa xenon gas in a magnetic field of 0.83 T.

due to the SAG blocks. In total, 16 PLS were measured, and the net counts for each set were typically 2×10^7. We determined ${}_1Z_{\mathrm{eff}}^{\mathrm{sc}}$ and ${}_1Z_{\mathrm{eff}}^{\mathrm{po}}$ due to the xenon gas at each temperature by comparing the two lifetimes at $B = 0.83$ and 0.00 T.

In a magnetic field, $|1,0\rangle$ and $|0,0\rangle$ states mix with each other, i.e., Zeeman mixing, to create two new Ps ground states:

$$\begin{aligned}|+\rangle &= (1/\sqrt{1+y^2})|1,0\rangle - (y/\sqrt{1+y^2})|0,0\rangle, \quad \text{and} \\ |-\rangle &= (y/\sqrt{1+y^2})|1,0\rangle + (1/\sqrt{1+y^2})|0,0\rangle, \qquad (11)\end{aligned}$$

where $y = x/(\sqrt{1+x^2}+1)$, and $x = 4\mu_0 B/\Delta_{\mathrm{HFS}}$. $\Delta_{\mathrm{HFS}} = 841\ \mu\mathrm{eV}$ is the hyperfine splitting between o-Ps and p-Ps. When $B \to 0$, one obtains $|+\rangle \to |1,0\rangle$ and $|-\rangle \to |0,0\rangle$. The lifetime of $|+\rangle$ is considerably shorter than that of $|1,\pm1\rangle$ because it can decay into two gamma-ray photons. For example, in a magnetic field of $B = 0.83$ T, the mixing rate of $|1,0\rangle$ in $|+\rangle$ is only 1%; however, the lifetime of $|+\rangle$ is 9.3 ns which is only $\frac{1}{15}$ of those of $|1,\pm1\rangle$. Therefore, the long lifetime is reduced in a magnetic field by the spin-conversion reaction from $|1,\pm1\rangle$ to $|+\rangle$, and the reaction rates can be deduced from this lifetime reduction [22,23,32].

IV. RESULTS AND DISCUSSION

A. Measurements

Figure 2 shows three PLS measured at 623 K. First, the long lifetime without xenon gas was found to be 128.7 ± 0.3 ns, which was shorter than the o-Ps lifetime in vacuum because of the POA due to the SAG blocks. Second, we introduced xenon gas at 250 kPa into the chamber, and the long lifetime was reduced to 85.8 ± 0.3 ns. This reduction occurred because of both POA and SCA due to the xenon gas. Third, we applied a magnetic field of 0.83 T, and the long lifetime was further reduced to 70.4 ± 0.5 ns. This further reduction occurred because of the spin-conversion reactions from $|1,\pm1\rangle$ to $|+\rangle$. From these results, the normalized annihilation rates at 623 K were found to be ${}_1Z_{\mathrm{eff}}^{\mathrm{sc}} = 3.11 \pm 0.14$ and ${}_1Z_{\mathrm{eff}}^{\mathrm{po}} = 1.36 \pm 0.17$, respectively. Thus, SCA accounted for 70% of the Ps annihilations due to Ps-Xe interactions at 623 K.

TABLE I. Fitting parameters obtained using the lowest three partial waves for Eq. (8). All values are in Hartree atomic units.

A_0	r_0	A_1	r_1	A_2
2.06 ± 0.10	16.2 ± 0.8	182 ± 21	-0.389 ± 0.018	290 ± 98
r_2	f_{sc} $(\times 10^{-6})$	f_{po} $(\times 10^{-7})$	d	
0.96 ± 0.17	2.82 ± 0.21	8.37 ± 0.30	2.39 ± 0.56	

We determined the annihilation rates at the other seven temperatures in the same way, and they are plotted in Fig. 3(a). The annihilation rates at 300, 423, 540, 588, and 623 K are consistent with our previous data within the statistical uncertainties. Those at 363, 483, and 510 K are measured for the present analysis.

In addition, we also take an experimental value of the Ps-Xe momentum-transfer cross section, found to be $\sigma_{\mathrm{m}}^{\mathrm{ex}} = (12 \pm 2) \times 10^{-20}\ \mathrm{m}^2$ at the Ps kinetic energy range 40–60 meV in our previous report [11], into consideration in the following partial-wave analysis.

B. Annihilation rates

We analyzed the measured energy dependence of the annihilation rates, ${}_1Z_{\mathrm{eff}}^{\mathrm{sc}}$ and ${}_1Z_{\mathrm{eff}}^{\mathrm{po}}$, and the experimentally determined momentum-transfer cross section [11] by using Eqs. (7) and (8) with nine fitting parameters (A_0, r_0, A_1, r_1, A_2, r_2, f_{sc}, f_{po}, and d), taking into account the three lowest partial waves ($L \leqslant 2$). The quantity γ^4 in Eq. (6) is fixed at 460 [27,29]. The nine parameters determined via a least-squares fitting are summarized in Table I. The uncertainties result from the statistical uncertainties of the measured data.

We have found that this calculation does not converge when using the two lowest partial waves ($L \leqslant 1$) or the four lowest partial waves ($L \leqslant 3$) because of the numbers of the fitting parameters to be determined from the measured data being too few or too many.

Figure 3(a) shows the fitted curves for the annihilation rates, ${}_1Z_{\mathrm{eff}}^{\mathrm{sc}}$ and ${}_1Z_{\mathrm{eff}}^{\mathrm{po}}$, calculated using Eq. (8) and the parameters in Table I. The curve for ${}_1Z_{\mathrm{eff}}^{\mathrm{po}}$ comprises *s*-, *p*-, and *d*-wave components, whereas the curve for ${}_1Z_{\mathrm{eff}}^{\mathrm{sc}}$ comprises *p*- and *d*-wave components. The two fitting curves share seven of the nine parameters (A_0, r_0, A_1, r_1, A_2, r_2, and d), and they agree well with the measurement points. These good agreements show that the temperature dependences of ${}_1Z_{\mathrm{eff}}^{\mathrm{sc}}$ and ${}_1Z_{\mathrm{eff}}^{\mathrm{po}}$ are well accounted for by the *s*-, *p*-, and *d*-wave contributions. There is no need to assume unknown annihilation paths other than SCA and POA to explain the abnormally strong temperature dependence of ${}_1Z_{\mathrm{eff}}^{\mathrm{po}}$, which increases by 160% when the temperature is elevated from 300 to 623 K [32]. This increase is considered rapid in comparison with those for helium, neon, argon, nitrogen, isobutane, neopentane, or methane, which exhibit 5%–25% increases when the temperature is elevated from 300 to 600 K [12,13].

Figure 3(b) shows the *s*-, *p*- and *d*-wave contributions to ${}_1Z_{\mathrm{eff}}^{\mathrm{po}}$. The ratios are 64.2%, 33.6%, and 2.2%, respectively, at 300 K. The *p*-wave contribution is not negligible even at room temperature. At 623 K, the corresponding contributions are 38.8%, 33.0%, and 28.0%, respectively. The 160% increase in ${}_1Z_{\mathrm{eff}}^{\mathrm{po}}$ is attributed not only to the increase in the *p*-wave

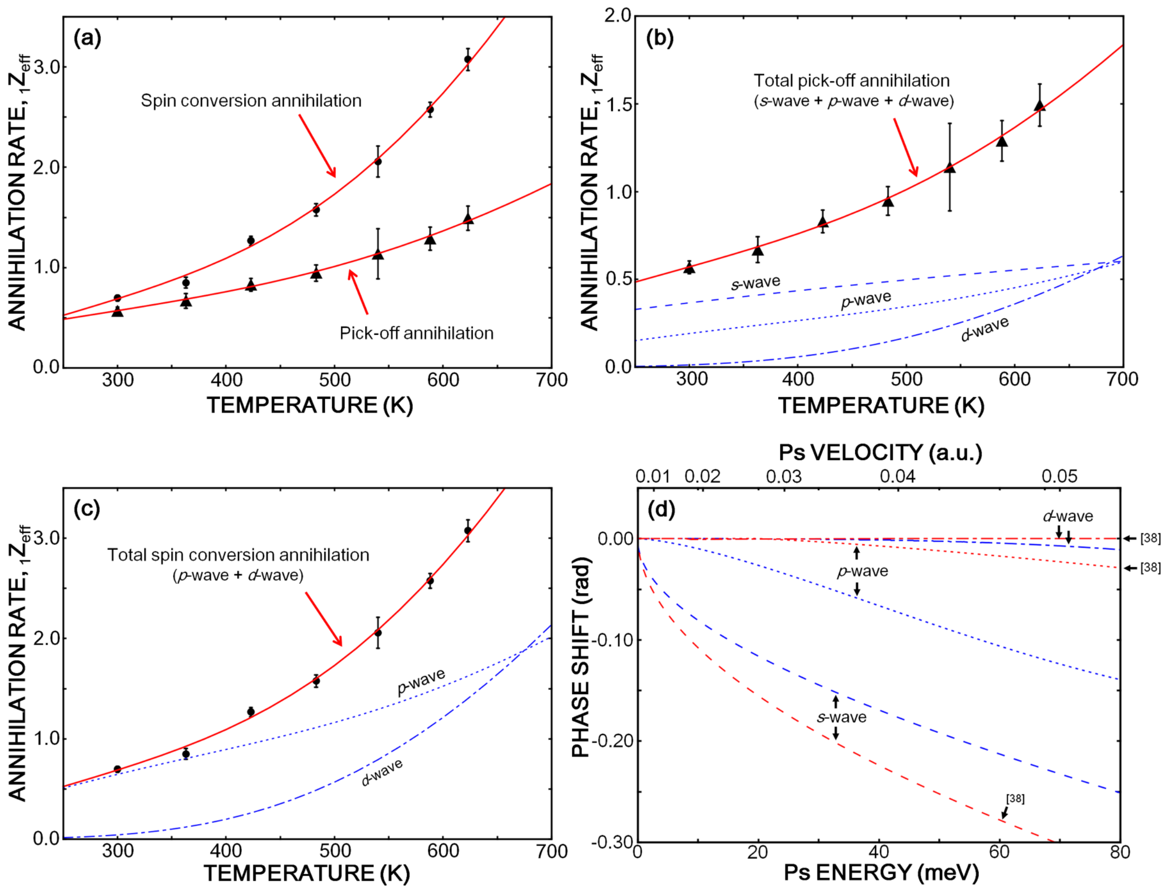

FIG. 3. (a) Temperature dependences of the normalized Ps annihilation rates: the measured points are $_1Z_{\text{eff}}^{\text{sc}}$ (circles) and $_1Z_{\text{eff}}^{\text{po}}$ (triangles), and the fitted lines (solid lines) are calculated using Eqs. (8) and the collisional parameters listed in Table I. (b) The fit for $_1Z_{\text{eff}}^{\text{po}}$ (solid line) and the contributions of the partial waves: the s wave (dashed line), p wave (dotted line), and d wave (dash-dotted line). (c) The fit curve for $_1Z_{\text{eff}}^{\text{sc}}$ (solid line) and the contributions of the partial waves: the p wave (dotted line) and d wave (dash-dotted line); the s-wave contribution is not shown because it is forbidden in SCA. (d) Phase shifts in the s-, p-, and d-wave scatterings as functions of energy (lower x axis) and velocity (upper x axis) as calculated using Eq. (6) and the parameters in Table I (blue lines) and as calculated by Gribakin *et al.* [38] (red lines). Note that "temperature" in (a)–(c) indicates that the Ps velocity distribution was considered by convolving with the Maxwell-Boltzmann distribution, whereas "energy" in (d) indicates that the Ps velocity distribution was not considered.

contribution but also to that of the d-wave contributions, whereas the increase in the s-wave contribution is rather moderate.

Figure 3(c) shows the p- and d-wave contributions to $_1Z_{\text{eff}}^{\text{sc}}$; the contribution of the s wave is not shown because it is forbidden in SCA. The shapes of the p- and d-wave contributions are the same as those in Fig. 3(b); however, the scales are changed by a factor of $f_{\text{sc}}/f_{\text{po}}$. The values of f_{sc} and f_{po} indicate that SCA occurs per $f_{\text{sc}}^{-1} = 3.5 \times 10^5$ collisions with $L \geqslant 1$ and that POA occurs per $f_{\text{po}}^{-1} = 1.2 \times 10^6$ collisions with any value of L.

Gribakin *et al.* [38] recently computed the scattering length to be $A_0^{\text{pp}} = 2.45\,a_0$ by the pseudopotential method including the van der Waals potential. The same authors presented another value of $A_0^{\text{s}} = 3.57\,a_0$ by the static approximation without taking account of the van der Waals interaction. This A_0^{s} is considerably larger than their A_0^{pp}, but it is close to $A_0^{\text{se}} = 3.77\,a_0$ obtained by Blackwood *et al.* [39] by the R-matrix method with the static-exchange approximation. In addition, Mitroy and Bromley [40] have calculated the scattering length and effective range by a fixed core stochastic variation method with model polarization potentials. Their values for positron-dominated scattering, electron-dominated scattering, and their average (neutral) are $(A_0^+, r_0^+) = (1.50, 9.61)$, $(A_0^-, r_0^-) = (2.60, 3.38)$, and $(A_0^{\text{av}}, r_0^{\text{av}}) = (2.29, 4.03)$, respectively. Our values of $(A_0^{\text{ex}}, r_0^{\text{ex}}) = (2.06, 16.2)$ are closer to (A_0^+, r_0^+) rather than to (A_0^-, r_0^-), which suggests that the positron plays the more important role during Ps-Xe collisions in the ultralow-energy region. This differs from the understanding that electron exchange plays the dominant role in the intermediate-energy region [8].

The small positive value of A_0 indicates that the xenon potential is weakly repulsive for Ps. As Gribakin *et al.* have shown via two kinds of calculations, the van der Waals interaction partly cancels the repulsion to make A_0 smaller, but the interaction is too weak to make it negative. This is consistent with the fact that Ps bubbles form in liquid xenon because of repulsive Ps-Xe interactions [41].

The present findings are the first experimental results for Ps collisions in the ultralow-energy region to determine the

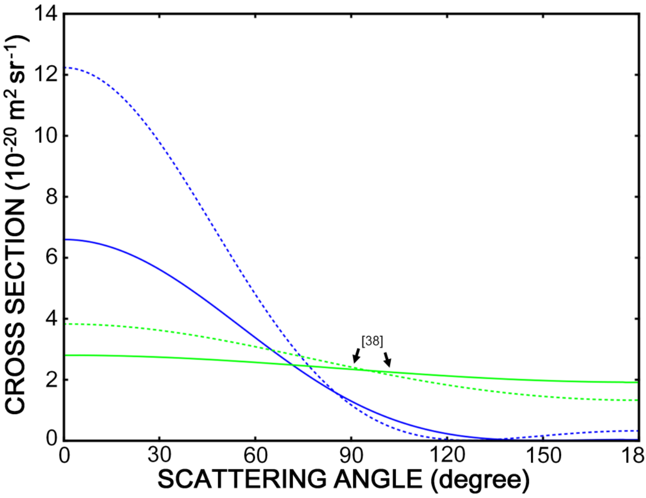

FIG. 4. Differential elastic scattering cross sections at energies of 40 meV (solid lines) and 80 meV (dotted lines), respectively. The two blue lines were calculated using Eq. (10), and the two green lines were calculated by Gribakin *et al.* [38].

p- and d- wave collisional parameters. The sensitivity of ${}_1Z_{\mathrm{eff}}^{\mathrm{sc}}$ to p- and d-wave scatterings is a noticeable advantage of the present method in comparison to low-energy electron-scattering experiments [24,25]. There have been few experimental or theoretical determinations of the p- and d- wave collisional parameters to compare with our results.

C. Phase shifts

Figure 3(d) shows the phase shifts of s-, p-, and d-wave scatterings as functions of energy and of the Ps velocity. The s-wave phase shift exhibits a rather moderate trend over this energy region, which is roughly similar to that obtained by Gribakin *et al.* [38]. The d-wave phase shift is very small, which is also similar to their result.

However, a major difference arises in the p-wave phase shift. We find a significant contribution, whereas the literature indicates only a small contribution in this energy range [38]. In support of our results, we note that a large phase shift in $L \geqslant 1$ scatterings are required because of the following two reasons: First, there is noticeable SCA even at room temperature (40 meV), which is forbidden in s-wave scattering. Second, there is the rapid increase in the POA rate, ${}_1Z_{\mathrm{eff}}^{\mathrm{po}}$, when the temperature is elevated from 300 to 623 K, which cannot be explained by s-wave nature.

D. Differential cross sections

Figure 4 shows the differential cross sections of the partial waves with $L \leqslant 2$ calculated using Eq. (10) at energies of 40 and 80 meV. The curves are not isotropic mainly because of the non-negligible p-wave contribution in Ps-Xe collisions even at room temperature. This anisotropy is consistent with the noticeable observation of SCA at these energies. We attribute the difference between the total and momentum-transfer cross sections described below, $\sigma_{\mathrm{T}} > \sigma_{\mathrm{m}}$, to the high fraction of the forward scattering. In contrast, Gribakin *et al.* have found relatively isotropic angular distributions [38], which correspond to the small phase shifts of the p- and d-waves they found at these energies.

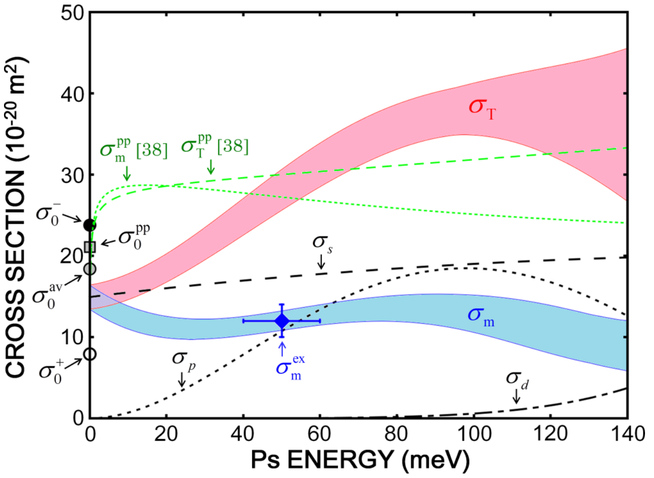

FIG. 5. The total cross section (σ_{T}), momentum-transfer cross section (σ_{m}), and partial cross sections of the s wave (σ_s: black dashed line), p wave (σ_p: black dotted line), and d wave (σ_d: black dash-dotted line) in Ps-Xe collisions calculated using the parameters listed in Table I. The bandwidths of σ_{T} and σ_{m} indicate the uncertainties. Our previous value of $\sigma_{\mathrm{m}}^{\mathrm{ex}}$ is indicated by a diamond (blue) with error bars [11]. The theoretical total cross section ($\sigma_{\mathrm{T}}^{\mathrm{pp}}$, green dashed line) and momentum-transfer cross section ($\sigma_{\mathrm{m}}^{\mathrm{pp}}$, green dotted line) by Gribakin *et al.* [38] are also displayed. The theoretical cross sections for $k \rightarrow 0$ by Gribakin *et al.* (σ_0^{pp}: shaded square) and by Mitroy and Bromley [40] for positron-dominated scattering (σ_0^+: open circle) and electron-dominated scattering (σ_0^-: closed circle), and the average (σ_0^{av}: shaded circle) are also displayed on the y axis.

E. Total and momentum-transfer cross sections

Figure 5 shows the total cross section, the momentum-transfer cross section, and the partial-wave scattering cross sections calculated using Eq. (7). The bandwidths of the total and momentum-transfer cross sections indicate the uncertainties [one standard deviation, $\Delta\sigma(k)$] that arise from the uncertainties in the collisional parameters listed in Table I:

$$\begin{aligned}
[\Delta\sigma(k)]^2 = {} & [\sigma(k,A_0+\Delta A_0,r_0,A_1,r_1,A_2,r_2,d) - \sigma(k,A_0,r_0,A_1,r_1,A_2,r_2,d)]^2 \\
& + [\sigma(k,A_0,r_0+\Delta r_0,A_1,r_1,A_2,r_2,d) - \sigma(k,A_0,r_0,A_1,r_1,A_2,r_2,d)]^2 \\
& + \cdots + [\sigma(k,A_0,r_0,A_1,r_1,A_2,r_2,d+\Delta d) - \sigma(k,A_0,r_0,A_1,r_1,A_2,r_2,d)]^2. \qquad (12)
\end{aligned}$$

The *d*-wave contributions in Figs. 3(b) and 3(c) appear larger than those in Fig. 5. This is due to the Ps energy distribution in thermal equilibrium given by Eq. (9); the Ps atoms in the higher-energy tail of the Maxwell-Boltzmann distribution play significant roles in the annihilation rates in Figs. 3(b) and 3(c).

In previous experiments [11], we obtained the momentum-transfer cross section $\sigma_{\mathrm{m}}^{\mathrm{ex}} = 12(2) \times 10^{-20}$ m^2 at energies of 40–60 meV, and we have taken this value into consideration in the present partial-wave analysis; it is also displayed in Fig. 5 with error bars.

The cross section at the zero-energy limit ($k \to 0$) obtained using the scattering length of $A_0^{\mathrm{pp}} = 2.45\,a_0$ of Gribakin *et al.* [38], e.g., $\sigma_0^{\mathrm{pp}} = 4\pi(A_0^{\mathrm{pp}})^2 = 21.1 \times 10^{-20}\,\mathrm{m}^2$, is also plotted in Fig. 5. Moreover, the total cross sections at $k \to 0$ by Mitroy and Bromley [27] are also plotted in Fig. 5: $\sigma_0^{\mathrm{av}} = 20.9 \times 10^{-20}\,\mathrm{m}^2$, $\sigma_0^{+} = 9.00 \times 10^{-20}\,\mathrm{m}^2$, and $\sigma_0^{-} = 27.1 \times 10^{-20}\,\mathrm{m}^2$, which correspond to $(A_0^{\mathrm{av}}, r_0^{\mathrm{av}})$, (A_0^{+}, r_0^{+}), and (A_0^{-}, r_0^{-}), respectively. Our total cross section at $k \to 0$, $\sigma_0^{\mathrm{ex}} = (15 \pm 2) \times 10^{-20}$ m^2, is an intermediate value between their values of σ_0^{av} and σ_0^{+}, and it is considerably different from σ_0^{-}. This indicates that the positron plays a more important role than the electron in Ps-Xe collisions in the ultralow-energy region, whereas the positron acts like a "spectator particle" in the intermediate energy region (1-100 eV).

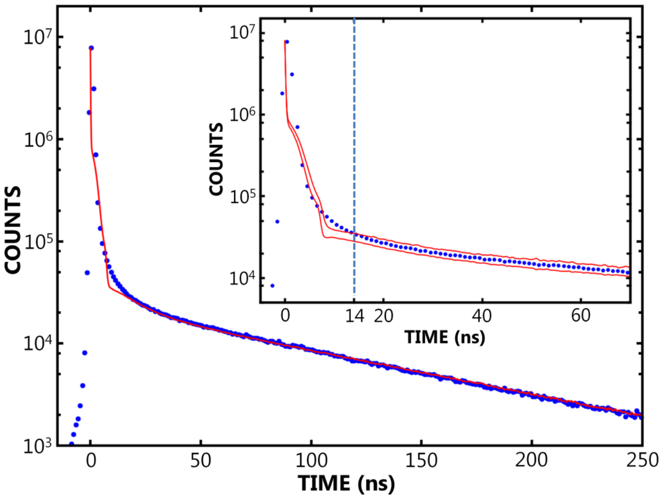

FIG. 7. The measured positron lifetime spectrum (blue circles) and the simulation (red solid line) assuming $M_{\mathrm{SAG}} = 60$. The inset is an enlarged view at a time earlier than 70 ns with the measured points (blue circle) together with two curves (red solid lines) indicating the uncertainties due to the uncertainties in the collisional parameters. After 14 ns (the vertical dashed line) the simulated spectrum agrees with the measured points within the uncertainties.

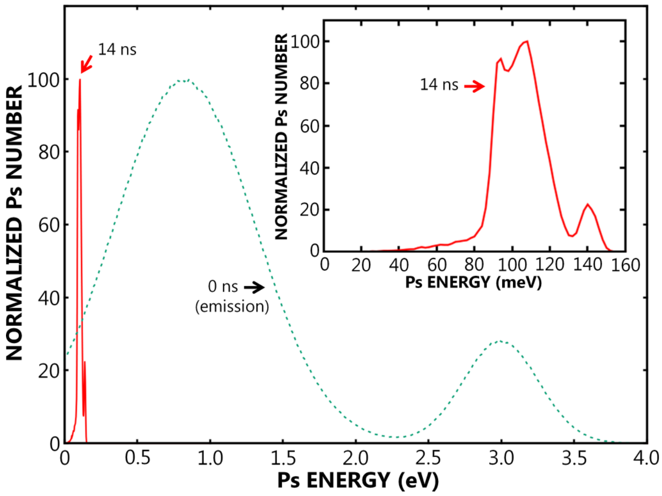

FIG. 6. The initial Ps energy distribution upon emission from the silica aerogel (dotted line) and the distribution at 14 ns (solid line) in 250-kPa gaseous xenon and silica aerogel at 300 K. The inset is an enlarged view for energies less than 160 meV.

F. Simulation of positron lifetime spectrum

To verify the fitting parameters listed in Table I, we have simulated the PLS at 300 K in 250-kPa gaseous xenon and SAG blocks and have compared it to the measured result. The initial Ps energy distribution upon the emission from the SAG is assumed to have two components: 0.8 ± 0.5 eV from the surfaces of the SAG and 3.0 ± 0.3 eV from inside of the SAG [35,42]. Their ratio of those emissions is 86:14, as shown in Fig. 6. The energetic Ps atoms lose kinetic energy via collisions with the xenon atoms and the SAG surfaces. The energy losses are assumed to be

$$\frac{dE}{dt} = -2m_{\mathrm{Ps}}v_{\mathrm{Ps}}\left(\frac{\sigma_{\mathrm{m}}n}{M_{\mathrm{Xe}}} + \frac{1}{\bar{l}M_{\mathrm{SAG}}}\right)(E - E_{\mathrm{th}}), \tag{13}$$

where $E = \hbar^2k^2/2m_{\mathrm{Ps}}$ is the Ps kinetic energy, m_{Ps} is the mass of a positronium atom, $v_{\mathrm{Ps}} = \hbar k/m_{\mathrm{Ps}}$ is the Ps velocity, n is the number density of xenon atoms, M_{Xe} is the mass of a xenon atom, $\bar{l}$ (= 70 nm) is the mean distance between SAG grains, M_{SAG} is the effective mass of the SAG surface atoms, and $E_{\mathrm{th}} = 3k_BT/2$ is the thermal energy [17,35]. We calculated $\sigma_{\mathrm{m}}(E)$ using Eq. (7b).

Figure 7 shows the simulated PLS. The simulation fits the data best when we assume $M_{\mathrm{SAG}} = 60$. The fact that M_{SAG} is larger than the mass of a single atom in the SAG, e.g., 16.0 for an oxygen atom or 28.1 for a silicon atom, implies that the Ps atom does not collide with a single atom but with an atomic group at the SAG surface, even though a Ps atom is as small as a hydrogen atom. A Ps atom exhibits a wave nature rather than a particle nature during collisions with the SAG surface in the ultralow-energy region.

The PLS simulation agrees well with the measurement points. In particular, no discrepancies exist beyond the statistical uncertainties in the time range after 14 ns. The average Ps energy at 14 ns is 100 meV, as shown in Fig. 6. Therefore, the fitted results shown in Figs. 3(a)–3(c) can be safely extrapolated at least up to 100 meV. The discrepancies prior to 14 ns may arise from the energy dependence of the energy loss per collision at the SAG surface. Some modifications to Eq. (13) may be required. For example, Nagashima *et al.* have suggested a strong energy dependence, such as $-dE/dt \propto E^{2.2} \propto E^{1.7}v_{\mathrm{Ps}}$ for SAG collisions [17]. In addition, the prompt decay is too steep as shown in the inset of Fig. 7. This suggests that the Ps-Xe scattering cross sections may be overestimated during the first 2 ns.

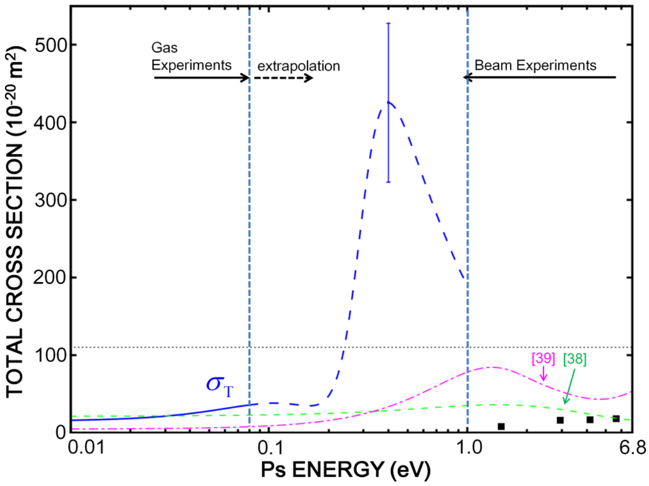

FIG. 8. The total cross section in Ps-Xe collisions, below the energy of the Ps ionizing threshold, calculated using the parameters listed in Table I and Eq. (7) (blue solid line). The extrapolation up to 0.1 eV is verified by the positron lifetime spectrum simulation (Fig. 7). Further extrapolation up to 1.0 eV (blue broken line) predicts a peak at the energy of 0.4 eV. The error bar indicates the uncertainty of the peak amplitude. Beam experiment results by Brawley *et al.* [7] (squares), together with the theoretical results by Gribakin *et al.* (green dashed line [38]) and by Blackwood *et al.* (magenta dash-dotted line [39]) are displayed. The horizontal line at 110×10^{-20} m^2 indicates the least value of the peak amplitude of σ_T obtained from the PLS simulation shown in Fig. 9. The numerical data of the total cross section are available in the Supplemental Material [47].

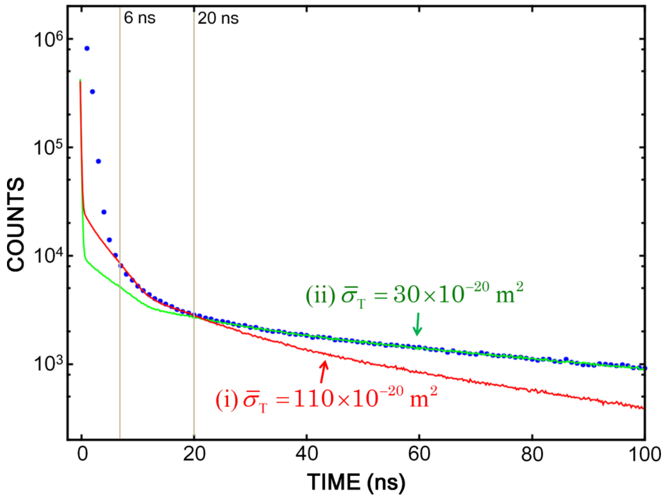

FIG. 9. Measured positron lifetime spectrum (blue circles) and simulated spectra assuming an energy-independent total scattering cross section of 110×10^{-20} m^2 [line (i)] or 30×10^{-20} m^2 [line (ii)]. The former simulation agrees well with the measured spectrum in the time range of 6–20 ns, whereas the latter simulation agrees well with the measured spectrum in the time range of after 20 ns. The two vertical lines mark the times of 6 and 20 ns. Both simulations calculate 10^7 Ps atoms and the results are multiplied by a factor of 0.185 and 0.204, respectively, to adjust the vertical scales.

G. Extrapolation to the inaccessible region

Further extrapolation above 100 meV is of great interest. Figure 8 shows the extrapolation of σ_T in Eq. (7) up to 1.0 eV. This predicts a peak in σ_T in Ps-Xe collisions near 0.4 eV. The contributions of the *s*-, *p*-, and *d*-wave scatterings at the peak are 4.5%, 37.1%, and 58.4%, respectively. As also shown in Fig. 8, beam experiments down to 1.0 eV have recently found a drop in σ_T at 1.3 eV [7], which may suggest the existence of a Ramsauer-Townsend minimum near this energy. In contrast, our analysis indicates that the scattering length in the Ps-Xe collisions has a small positive value, so there should not be a Ramsauer-Townsend minimum but rather a peak at approximately 0.4 eV. The *s*-wave cross section, by itself, possesses a minimum near 1.0 eV where $\delta_0 = 0$; however, this valley is filled with the larger contributions of the *p*- and *d*-wave cross sections. Consequently, a Ramsauer-Townsend minimum should not appear in Ps-Xe collisions. Similar structures due to positive values of A_0 have been found in calculations for Ps-Xe, Ps-Kr, and Ps-Ar scatterings [8,38] and for electron-neon scattering [43].

This prediction of the existence of a peak in σ_T near 0.4 eV, which is dominated by *p*- and *d*-wave components, is qualitatively supported by the fact that an increase in collisional annihilation below 1.0 eV is a necessary condition to yield the fast component observed near the prompt peak of the PLS in gaseous xenon [44]. In other words, most of the young and energetic Ps atoms must annihilate with a large cross section before their thermalization in xenon. This phenomenon has been called the "Xe problem," where the positronium formation fraction in gaseous xenon appears to be much less than that in gaseous helium [9,45]. This problem certainly results from SCA, due to spin-orbit interactions with high-Z atoms, whose cross sections possess a strong energy dependence. This reaction is allowed in $L \geqslant 1$ scatterings, which are dominantly responsible for the σ_T peak near 0.4 eV.

As shown in Fig. 8, the peak amplitude of the extrapolated σ_T is estimated to be $(430 \pm 100) \times 10^{-20}$ m^2. This value is five or more times larger than a value of 40×10^{-20} m^2 given by Gribakin *et al.* [38] at a Ps velocity of 0.23 a.u. (1.4 eV) or a value of 90×10^{-20} m^2 given by Blackwood *et al.* [39] at a Ps velocity of 0.22 a.u. (1.3 eV).

In an effort to understand the discrepancy, we have performed simple PLS simulations using fixed, energy-independent values of the momentum-transfer cross section, the total scattering cross section, and the annihilation rates per collision throughout the time from the emission to the annihilation of Ps. We fixed the momentum-transfer cross section at $\bar{\sigma}_m = \sigma_m^{ex} = 12 \times 10^{-20}$ m^2 [11], and we fixed the annihilation rates per collision at $f_{sc} = 2.82 \times 10^{-6}$ and $f_{po} = 8.37 \times 10^{-7}$ as in Table I.

We simulated several sets of PLS with the σ_T fixed at various values, and we found that, as shown in Fig. 9, one simulation using the value of $\bar{\sigma}_T = 110 \times 10^{-20}$ m^2 agrees well with the measured PLS in the time range of 6–20 ns [line (i)], whereas another simulation using a different value of $\bar{\sigma}_T = 30 \times 10^{-20}$ m^2 agrees well with the measured PLS in the time range after 20 ns [line (ii)]. These agreements indicate that the average value of σ_T in the time range of 6–20 ns is 110×10^{-20} m^2, whereas that in the time range after 20 ns is

30×10^{-20} m^2. Accordingly, the maximum value of σ_T must be larger than 110×10^{-20} m^2.

We can, therefore, conclude that the peak amplitude of σ_T lies between 110×10^{-20} m^2 and $(430 \pm 100) \times 10^{-20}$ m^2. The latter value was obtained on the basis of the parameters in Table I and Eq. (7). As mentioned above in regard to Fig. 7, we may overestimate σ_T in the first 2 ns. On the other hand, the former value is supported by the simulations in Fig. 9. This value, 110×10^{-20} m^2, is a lower limit to the peak value and is shown in Fig. 8 as a horizontal dotted line. This value is 30% larger than a peak value calculated by Blackwood *et al.* [39] (85×10^{-20} m^2) and three times larger than a peak value calculated by Gribakin *et al.* [38] (36×10^{-20} m^2). The remaining discrepancy will be investigated in future experimental and theoretical works. Improvements in Ps beam techniques are strongly desired [7,46].

The present simulations indicate that the Xe problem occurs because of a peak in σ_T at approximately 0.4 eV with an amplitude of more than 110×10^{-20} m^2. This causes most Ps atoms to annihilate before thermalization via the ortho-para spin-conversion reaction during Ps-Xe collisions with $L \geqslant 1$.

V. CONCLUSIONS

In this paper, we have proposed an analytical method based on a partial-wave expansion to convert Ps annihilation rates into total cross sections during Ps-Xe collisions. We found the scattering length and effective range to be $A_0 = 2.06\,a_0$ and $r_0 = 16.2\,a_0$, respectively. These values indicate that the positron plays a more important role than the electron in the ultralow-energy region of less than 100 meV. The xenon potential is repulsive for Ps because the van der Waals interaction is too weak to make A_0 negative. Consequently, a Ramsauer-Townsend minimum should not appear in the Ps-Xe collisions. A rough determination made by extrapolating the analytical results up to 1 eV, where experimental access has not been achieved yet, indicates that there would be a peak in the total cross section near an energy of 0.4 eV which can be attributed to the fast component observed in PLS in gaseous xenon.

ACKNOWLEDGMENTS

The authors gratefully acknowledge the financial support of JSPS KAKENHI grants (Grant No. 16K17771 to K.S. and Grant No. 15H03703 to H.S.).

[1] M. Charlton and J. W. Humberston, *Positron Physics* (Cambridge University Press, Cambridge, UK, 2001).

[2] G. F. Gribakin, J. A. Young, and C. M. Surko, Rev. Mod. Phys. **82**, 2557 (2010).

[3] G. Laricchia and H. R. J. Walters, Riv. Nuovo Cimento **35**, 305 (2012).

[4] K. Fedus, G. P. Karwasz, and Z. Idziaszek, Phys. Rev. A **88**, 012704 (2013).

[5] S. J. Brawley, S. Armitage, J. Beale, D. E. Leslie, A. I. Williams, and G. Laricchia, Science **330**, 789 (2010).

[6] S. J. Brawley, A. I. Williams, M. Shipman, and G. Laricchia, J. Phys.: Conf. Series **388**, 012018 (2012).

[7] S. J. Brawley, S. E. Fayer, M. Shipman, and G. Laricchia, Phys. Rev. Lett. **115**, 223201 (2015).

[8] I. I. Fabrikant and G. F. Gribakin, Phys. Rev. Lett. **112**, 243201 (2014).

[9] M. Tuomisaari, K. Rytsola, and P. Hautojarvi, J. Phys. B **21**, 3917 (1988).

[10] K. Wada, F. Saito, and T. Hyodo, Phys. Rev. A **81**, 062710 (2010).

[11] K. Shibuya, Y. Kawamura, and H. Saito, Phys. Rev. A **88**, 042517 (2013).

[12] M. Skalsey, J. J. Engbrecht, R. K. Bithell, R. S. Vallery, and D. W. Gidley, Phys. Rev. Lett. **80**, 3727 (1998).

[13] M. Skalsey, J. J. Engbrecht, C. M. Nakamura, R. S. Vallery, and D. W. Gidley, Phys. Rev. A **67**, 022504 (2003).

[14] J. J. Engbrecht, M. J. Erickson, C. P. Johnson, A. J. Kolan, A. E. Legard, S. P. Lund, M. J. Nyflot, and J. D. Paulsen, Phys. Rev. A **77**, 012711 (2008).

[15] M. Kamimoto and T. Hyodo, J. Phys. B **21**, 2977 (1988).

[16] P. G. Coleman, S. Rayner, F. M. Jacobsen, M. Charlton, and R. N. West, J. Phys. B **27**, 981 (1994).

[17] Y. Nagashima, T. Hyodo, K. Fujiwara, and A. Ichikawa, J. Phys. B **31**, 329 (1998).

[18] F. Saito, Y. Nagashima, and T. Hyodo, J. Phys. B **36**4191 (2003).

[19] R. E. Lingenfelter, J. C. Higdon, and R. E. Rothschild, Phys. Rev. Lett. **103**, 031301 (2009).

[20] F. Blanco, A. M. Roldán, K. Krupa, R. P. McEachran, R. D. White, S. Marjanović, Z. Lj Petrović, M. J. Brunger, J. R. Machacek, and S. J. Buckman, J. Phys. B **49**, 145001 (2016).

[21] J. Mitroy and S. A. Novikov, Phys. Rev. Lett. **90**, 183202 (2003).

[22] H. Saito and T. Hyodo, Phys. Rev. Lett. **97**, 253402 (2006).

[23] H. Saito, T. Nakayama, and T. Hyodo, J. Phys.: Conf. Ser. **194**, 012038 (2009).

[24] M. Kurokawa, M. Kitajima, K. Toyoshima, T. Kishino, T. Odagiri, H. Kato, M. Hoshino, H. Tanaka, and K. Ito, Phys. Rev. A **84**, 062717 (2011).

[25] M. Kitajima, M. Kurokawa, T. Kishino, K. Toyoshima, T. Odagiri, H. Kato, K. Anzai, M. Hoshino, H. Tanaka, and K. Ito, Eur. Phys. J. D **66**130 (2012).

[26] I. A. Ivanov, J. Mitroy, and K. Varga, Phys. Rev. A **65**, 032703 (2002).

[27] J. Mitroy and M. W. J. Bromley, Phys. Rev. A **68**, 035201 (2003).

[28] I. I. Fabrikant and G. F. Gribakin, Phys. Rev. A **90**, 052717 (2014).

[29] A. R. Swann, J. A. Ludlow, and G. F. Gribakin, Phys. Rev. A **92**, 012505 (2015).

[30] O. Hinckelmann and L. Spruch, Phys. Rev. A **3**, 642 (1971).

[31] P. S. Ganas, Phys. Rev. A **5**, 1684 (1972).

[32] K. Shibuya, T. Nakayama, H. Saito, and T. Hyodo, Phys. Rev. A **88**, 012511 (2013).

[33] S. Henning and L. Svensson, Phys. Scr. **23**, 697 (1981).

[34] G. Poelz and R. Riethmuller, Nucl. Instrum. Methods **195**, 491 (1982).

[35] Y. Nagashima, M. Kakimoto, T. Hyodo, K. Fujiwara, A. Ichimura, T. Chang, J. Deng, T. Akahane, T. Chiba, K. Suzuki, B. T. A. McKee, and A. T. Stewart, Phys. Rev. A **52**, 258 (1995).

[36] H. Saito, Y. Nagashima, T. Kurihara, and T. Hyodo, Nucl. Instrum. Methods Phys. Res., Sect. A **487**, 612 (2002).

[37] H. Saito and T. Hyodo, Radiat. Phys. Chem. **68**, 431 (2003).

[38] G. F. Gribakin, A. R. Swann, R. S. Wilde, and I. I. Fabrikant, J. Phys. B **49**, 064004 (2016).

[39] J. E. Blackwood, M. T. McAlinden, and H. R. J. Walters, J. Phys. B **36**, 797 (2003).

[40] J. Mitroy and M. W. J. Bromley, Phys. Rev. A **67**, 034502 (2003).

[41] P. G. Varlashkin, Phys. Rev. A **3**, 1230 (1971).

[42] Y. Nagashima, Y. Morinaka, T. Kurihara, Y. Nagai, T. Hyodo, T. Shidara, and K. Nakahara, Phys. Rev. B **58**, 12676 (1998).

[43] R. P. McEachran and A. D. Stauffer, J. Phys. B **16**, 4023 (1983).

[44] P. G. Coleman, T. C. Griffith, G. R. Heyland, and T. L. Killeen, J. Phys. B **8**, 1734 (1975).

[45] G. L. Wright, M. Charlton, T. C. Griffith, and G. R. Heyland, J. Phys. B **18**, 4327 (1985).

[46] K. Michishio, T. Tachibana, R. H. Suzuki, K. Wada, A. Yagishita, T. Hyodo, and Y. Nagashima, Appl. Phys. Lett. **100**, 254102 (2012).

[47] See Supplemental Material at http://link.aps.org/supplemental/10.1103/PhysRevA.97.052702 for the numerical data of the Ps-Xe total cross section and the uncertainty shown in Fig. 8.